CHEMISTRY OF MATERIALS

Article

pubs.acs.org/cm

Highly Fluorescent Ribonuclease-A-Encapsulated Lead Sulfide Quantum Dots for Ultrasensitive Fluorescence *in Vivo* Imaging in the Second Near-Infrared Window

Yifei Kong,[†] Jun Chen,[‡] Hongwei Fang,[§] George Heath,[∥] Yan Wo,[§] Weili Wang,[†] Yunxia Li,[‡] Yuan Guo,[†] Stephen D. Evans,[∥] Shiyi Chen,*[,‡] and Dejian Zhou*[,†]

[†]School of Chemistry and Astbury Structure for Molecular Biology, University of Leeds, Leeds LS2 9JT, United Kingdom

[‡]Department of Orthopedic Sports Medicine, Huashan Hospital Affiliated to Fudan University, Shanghai 200040, P. R. China

[§]Department of Human Anatomy, Histology and Embryology, School of Medicine, Shanghai Jiao Tong University, Shanghai 200025, P. R. China

[∥]School of Physics and Astronomy, University of Leeds, Leeds LS2 9JT, United Kingdom

Supporting Information

ABSTRACT: Ribonuclease-A (RNase-A) encapsulated PbS quantum dots (RNase-A@PbS Qdots) which emit in the second near-infrared biological window (NIR-II, *ca.* 1000−1400 nm) are rapidly synthesized under microwave heating. Photoluminescence (PL) spectra of the Qdots can be tuned across the entire NIR-II range by simply controlling synthesis temperature. The size and morphology of the Qdots are examined by transmission electron microscopy (TEM), atomic force microscopy (AFM), and dynamic light scattering (DLS). Quantum yield (Φ_f) measurement confirms that the prepared Qdots are one of the brightest water-soluble NIR-II emitters for *in vivo* imaging. Their high Φ_f (∼17.3%) and peak emission at ∼1300 nm ensure deep optical penetration to muscle tissues (up to 1.5 cm) and excellent imaging contrast at an extremely low threshold dose of ∼5.2 pmol (∼1 μg) per mouse. Importantly, this protein coated Qdot displays no signs of toxicity toward model neuron, normal, and cancer cells *in vitro*. In addition, the animal's metabolism results in thorough elimination of intravenously injected Qdots from the body within several days via the reticuloendothelial system (RES), which minimizes potential long-term toxicity *in vivo* from possible release of lead content. With a combination of attractive properties of high brightness, robust photostability, and excellent biocompatibility, this new NIR-II emitting Qdot is highly promising in accurate disease screening and diagnostic applications.

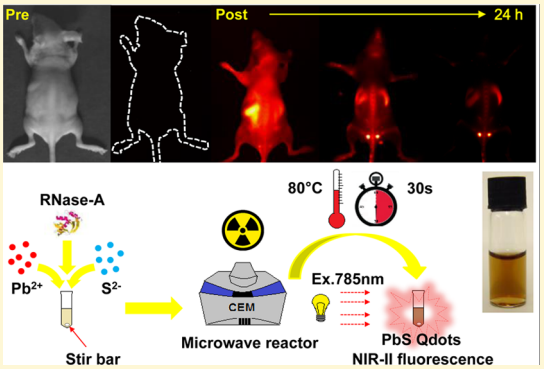

INTRODUCTION

Over the past 20 years, fluorescent semiconductor nanocrystals, also known as quantum dots (Qdots), have emerged as a powerful probe for biology because of their unique, size-dependent, bright, and stable fluorescence.[1−5] In particular, Qdots that emit in the second near-infrared biological window (NIR-II, 1000−1400 nm, photon energy 1.24−0.89 eV) are extremely attractive for *in vivo* fluorescence imaging. This is due to the greatly reduced light absorption and scattering together with nearly zero biological autofluorescence background, leading to the deepest light penetration into the body with significantly increased imaging contrast, fidelity, and resolution.[6−9] Compared to the widely used NIR-I emitters (*ca.* 650−900 nm), the NIR-II reporters can provide much higher imaging signal-to-noise (S/N) ratio and spatial resolution *in vivo*.[6−8,10−16] Thus far, myriad endeavors have been devoted to develop feasible NIR-II emitters for biomedical imaging applications. Notable examples are the single-walled carbon nanotubes (SWCNTs),[7,11,13] organic dyes (*e.g.*, ICG and IR-26),[17,18] and Qdots made of different low-bandgap materials (*e.g.*, PbS, PbSe, InAs, and CdHgTe).[8,14−16,18−26] Among which, Qdots exhibit superior optical properties such as narrow and size-tunable emission, high fluorescence quantum yield (Φ_f), and excellent robustness against photobleaching, making them well-suited for sensitive and long-term fluorescence imaging.

Since the Qdot bandgap (corresponding to its emitted photoenergy) is made of bulk bandgap and quantum confinement, it is hence normally greater than that of the corresponding bulk material. It is therefore unsurprising that all known NIR-II emitting Qdots are made of low-bandgap materials such as PbS (0.37 eV), PbSe (0.27 eV), PbTe (0.32

Received: January 18, 2016
Revised: April 5, 2016
Published: April 6, 2016

DOI: 10.1021/acs.chemmater.6b00208
Chem. Mater. 2016, 28, 3041−3050

eV), InAs (0.35 eV), HgS (0.30 eV), Ag_2S (1.05 eV), and Ag_2Se (0.15 eV), most of which contain malicious ingredients (Pb, As, Cd, and Hg). Moreover, they often suffer limitations such as low stability under ambient or biological environments (*e.g.*, prone to oxidation for PbSe, PbTe),[27] requiring high-temperature synthesis and postsynthesis modifications to achieve water-solubility, which often leads to significantly reduced Φ_f,[15] and/or difficulty in achieving size-dependent color tunability (*e.g.*, Ag_2S).[14] Therefore, the development of an effective aqueous synthesis route to high-quality, biocompatible NIR-II emitting Qdots is highly attractive for overcoming such limitations.[22,26] Indeed, several thiol-containing small-molecule ligands, including thiolglycerol, dihydrolipoic acid, L-cysteine, and glutathione (GSH), have been employed to synthesize NIR-II emitting PbS Qdots in aqueous media.[27] Unfortunately, such small-molecule ligands are unlikely to provide a dense, robust surface coating to impede leakage of toxic metal ions,[22] whereas proteins, with unique three-dimensional structures and multiple functional groups, can stabilize Qdots more effectively by providing a dense, biocompatible coating. Indeed, a few proteins, such as apoferritin,[20] luciferase,[28] and recombinant EGFP-protein G,[26] have been used to "trap" or "bio-mineralize" certain sized PbS Qdots. More interestingly, the PbS Qdot-bound luciferase proteins are functional for bioluminescence resonance energy transfer (BRET) studies.[28] In this regard, we have previously demonstrated that ribonuclease-A (RNase-A), a small monomeric protein (Mw ~13.7 kDa), can template the synthesis of highly fluorescent gold nanoclusters[29] and CdTe Qdots[30] for cellular imaging in the NIR-I and visible region, respectively. Herein, the RNase-A assisted synthesis approach is extended to regulate the formation of strongly fluorescent, color tunable, and biocompatible PbS Qdots for ultrasensitive *in vivo* fluorescence imaging in the attractive NIR-II window. Compared to other protein templates, RNase-A appears to be superior due to its high thermal stability (can sustain 100 °C without aggregation) and tininess, allowing for significantly reduced overall Qdot hydrodynamic diameter (D_h) to benefit rapid clearance from body and minimize potential toxicity *in vivo*. These are non-negligible factors for any heavy-metal-containing imaging agent.

EXPERIMENTAL SECTION

Reagents and Materials. All chemicals were used as received without further purification. Pure water (resistivity: 18.2 mΩ cm) was used to prepare working solutions and buffers. Bovine pancreatic ribonuclease A (MW: 13.7 kDa, >70 U/mg), lead acetate trihydrate ($Pb(OAc)_2{\cdot}3H_2O$, ≥99.9%), sodium sulfide nonahydrate ($Na_2S{\cdot}9H_2O$, ≥ 98.0%), and sodium hydroxide (NaOH, ≥ 98.0%) were purchased from Sigma-Aldrich. Fetal bovine serum (FBS) and Dulbecco's modified Eagle medium (DMEM) were ordered from Thermo Fisher Scientific. DHC-N01 C-chip disposable hemacytometer was used for cell counting.

Animals. All living nude mice of 4 weeks old (weight: 200−240 g) were provided by the Animal Care Facility of School of Medicine Shanghai Jiao Tong University (Shanghai, China). All animal experiments were strictly performed under the guidelines of the Chinese Council for Animal Care, approved by the Animal Care Committee of the Laboratory Animal at School of Medicine, Shanghai Jiao Tong University.

Instrumentation. Pure water was generated by an ELGA Purelab classic UVF system. Microwave synthesis was carried out in a microwave reactor (Discover, CEM). The photograph of as-prepared Qdots was captured using a SONY DSC-F717 digital camera prior to being purified with Amicon ultracentrifugal filter tubes (MWCO: 10 or 30 kDa). Centrifugations were performed with a Thermo Scientific Heraeus Fresco 21 microcentrifuge and/or an Eppendorf 5810R centrifuge. Absorption spectra were recorded on a LAMBDA 950 UV/vis/NIR spectrophotometer equipped with an indium gallium arsenide (InGaAs) 150 mm integrating sphere (PerkinElmer) over a wavelength range from 700 to 1700 nm. NIR-II fluorescence spectra were measured with a NS1 NanoSpectralyzer fluorimetric analyzer (Applied NanoFluorescence) with λ_{ex} = 785 nm. Morphological and structural data including transmission electron microscopy (TEM), high-angle annular dark-field scanning transmission electron microscopy (HAADF-STEM), selected area electron diffraction (SAED), and energy dispersive X-ray (EDX) analysis were obtained with a FEI Tecnai F20 field emission gun TEM/STEM microscope operated at 200 kV and fitted with a Fischione HAADF detector and an 80 mm^2 Oxford Instruments X-Max silicon drift detector (SDD) and a Gatan Orius SC600A CCD camera. Dynamic light scattering (DLS) analysis was conducted at a fixed scattering angle of 90° on a Malvern Zetasizer NanoSampler instrument. Atomic force microscopy (AFM) images were obtained using a Dimension FastScan BioAFM (Bruker). Phase-contrast and corresponding fluorescence pictures of rat cortical neuronal cells were captured with a LAS X Widefield system (Leica Microsystem). Flow cytometric analysis was performed using a FACSCalibur flow cytometry system (BD Bioscience). A home-built NIR-II imaging prototype coupled with a 2-dimensional InGaAs CCD camera was used to collect NIR-II images. An 808 nm diode laser was the excitation source with 850 and 1000 nm short-pass filters. The emission light was filtered by an 1100 long-pass filter before reaching the CCD detector. The percentage of injected dose (ID) of the Qdots per gram (g) of tissue over time was determined with an Agilent 7900 inductively coupled plasma-mass spectrometry (ICP-MS).

Preparation of RNase-A-Encapsulated PbS Qdots (RNase-A@PbS Qdots). A 50 μL portion of NaOH solution (1 M) was added dropwisely into 1 mL of RNase-A/Pb^{2+} precursor solution, prepared by mixing 500 μL of 50 mg/mL RNase-A with 500 μL of 10 mM $Pb(OAc)_2$, to basify the system pH to ~11. After the mixture stirred for 5 min, 200 μL of 10 mM Na_2S solution was added, and then the mixed solution was heated at 80 °C for 30 s in a microwave reactor with an input power of 30 W. The mixture rapidly changed from colorless into dark brown, suggesting the formation of PbS Qdots. The as-prepared Qdots were dialyzed against 1× PBS buffer (pH = 7.4) overnight to neutralize system pH and remove unreacted reagents (*e.g.*, Pb^{2+}, Na^+, OAc^-, *etc*). Thereafter, the resulting stock solution was stored at 4 °C in darkness.

Flow Cytometry (Cell Cycle and Apoptosis Analysis). Human gastric epithelial GES-1 cells (normal cells) were plated on 6-well tissue culture plate at a density of 2×10^6 cells per well overnight and then incubated with a complete DMEM medium or a Qdot-preconditioned medium with different concentrations (*i.e.*, 1.3, 2.6, 13, and 26 nM) for 24 h. Next, cells per well were transferred to a centrifuged tube, spun down to a pellet at ×1000 *g* for 5 min, washed, and resuspended in 2 mL of PBS and eventually divided into two halves (~1 mL for each). To assess cell cycle phase distribution, half of the cells were fixed by adding 4 mL of cold ethanol (95%) to 1 mL of cell suspension and incubated at 4 °C for 12 h. Thereafter, the cells were resuspended in 5 mL of PBS containing 1% fetal bovine serum (FBS), and stained with 0.4 μL of propidium iodide (PI) containing 1 μL of RNase-A (10 mg/mL) for 0.5 h. The resultant solution was stored at 4 °C in darkness. Cell cycle and phase distribution were analyzed using CellQuestPro and ModtFit LT 3.0 software. On the other hand, cell apoptosis and necrosis were assessed using an APC Annexin V/PI apoptosis detection kit (BD Biosciences). The other half of the cells were washed with cold PBS and resuspended in 1× binding buffer (0.01 M HEPES, 0.14 M NaCl, 2.5 mM $CaCl_2$, pH 7.4). Next, a 100 μL portion of the solution (~1×10^5 cells) was transferred to a 5 mL tube prior to the addition of 5 μL of APC Annexin V and 5 μL of PI (20 μg/mL). After 20 min incubation, apoptotic and necrotic cells were stained and distinguished depending on APC Annexin V reactivity and PI exclusion. At last, 400 μL of 1× binding buffer was added to the culture tube and analyzed within 1 h using the flow cytometry.

DOI: 10.1021/acs.chemmater.6b00208
Chem. Mater. 2016, 28, 3041−3050

Immunofluorescent Staining. After 24 h incubation in PBS, ~1 μM RNase-A@PbS Qdots or ~0.5 μM $Pb(OAc)_2$, three parallels of neuronal cells were fixed with 4% paraformaldehyde (PFA) for 1 h. After being washed in 0.01 M PBS, the cells were blocked with 10% normal goat serum (NGS) for 1 h, and then incubated with anti-β-tubulin primary antibody (1:100 dilution) for ~12 h at 4 °C. Afterward, the fixed cell cultures were washed three times with 0.01 M PBS and incubated with secondary antibody (against the primary antibody) for another 1 h at 37 °C in a heating bath. The cells were rinsed in 0.01 M PBS prior to incubation with a Hoechst solution (Hoechst 33342, 1:5000) for staining the nuclei. The anti-β-tubulin antibody specifically recognizes the fetal rat cortical neurons and nerve fibers. The morphology of neurons with a high correlation to lead toxicity was observed under an immunofluorescent microscope.

***In Vivo* Imaging.** All nude mice were raised under filtered air (temperature: 22 ± 2 °C; humidity: 55 ± 5%) in plastic cages with sterilized wood shavings for bedding, and fed with a standard pellet diet and tap water. For imaging applications, the animals had been anesthetized with 5% (v/w) chloral hydrate. After that, a 200 μL aliquot of RNase-A@PbS Qdots (~26 nM, dosage: ~1 μg per mouse) was intravenously injected into the tail vein. Immediately after the injection, the signal was recorded at various time points over a 24 h period. At last the mice were sacrificed to harvest their major organs for *ex vivo* imaging and H&E stain. An 808 nm diode laser with 850 and 1000 nm short-pass filters was used as the excitation source, and the power density was set at 15 mW/cm^2 with exposure time of 100 ms. In order to collect NIR-II fluorescence images with an InGaAs CCD camera, the emission signal was filtered by an 1100 nm long-pass filter.

RESULTS AND DISCUSSION

Synthesis of RNase-A@PbS Qdots. Scheme 1 describes the proposed reaction path for the synthesis of RNase-A encapsulated PbS (RNase-A@PbS) Qdots. Briefly, the precursors, *i.e.*, $Pb(OAc)_2$, RNase-A, and Na_2S solutions, are mixed up in a vessel that is sealed and then inserted in a microwave system. The reaction vessel is subjected to heating for 30 s under constant stirring, during which the Pb^{2+} cations and S^{2-} anions react with each other to form PbS nanocrystals whose surfaces are simultaneously capped by protein molecules to prevent macroscopic aggregation and/or precipitation. The aqueous synthesis completes rapidly, generating a uniform dark-brown suspension of RNase-A@PbS Qdots in 30 s (see inset photograph in Scheme 1). It is worth mentioning that microwave heating plays a critical role in the high-quality Qdot synthesis: those heated in a metal dry bath incubator under equivalent conditions yield much weaker fluorescence (by >11-fold) even after the heat treatment is prolonged to 15 min (see SI, Figure S1). Apparently the ability of reaching target temperature rapidly appears important to achieve high Qdot quality, a significant advantage of microwave assisted synthesis.[34]

Scheme 1. Schematic of RNase-A@PbS Qdot Synthesis under Microwave Irradiation[a]

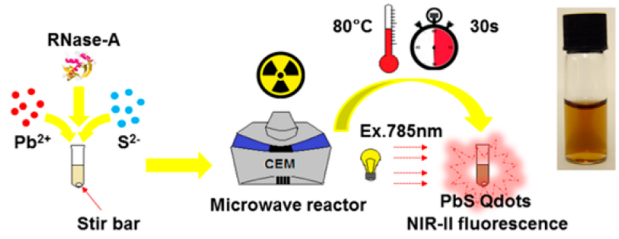

[a]Inset shows an optical photograph of freshly prepared RNase-A@PbS Qdots.

Fluorescence Spectra and Stability of RNase-A@PbS Qdots. Figure 1a shows fluorescence spectra of the as-prepared RNase-A@PbS Qdots (λ_{ex} = 785 nm). By changing reaction temperature, the emission maxima (λ_{em}) of the Qdots can be modulated systematically across the entire NIR-II region, from *ca.* 950 to 1300 nm. The Qdots prepared at 80 °C display an almost perfect Gaussian-shaped emission peaking at 1308 nm with a narrow full width at half-maximum (fwhm) of ~135 nm (Figure 1b). Such a fluorescence character should enable the deepest tissue penetration.[9,15] Hence, the 1308 nm emitting Qdots are the only candidate for follow-up experiments. The absorption spectrum of the Qdots increases monotonously toward the shorter wavelength with the first excitonic absorption peaking at 1260 nm, corresponding to the ground state excitonic transition energy (E_0) of 0.98 eV. By using the E_0 (in eV)−particle diameter (d, in nm) relationship for PbS Qdots reported by Moreels et al.,[31] the size of the Qdot can be calculated from eq 1:

$$E_0 = 0.41 + \frac{1}{0.0252d^2 + 0.283d} \quad (1)$$

Given E_0 = 0.98 eV, the diameter (d) of the PbS Qdot is calculated as 4.44 nm. Such a size matches perfectly to that measured by transmission electron microscopy (TEM, see the next section). Interestingly, the λ_{em} of the Qdots is red-shifted with the increasing temperature together with narrowing emission spectra (smaller fwhm), indicating the formation of larger and more uniform sized Qdots at higher synthesis temperatures (SI, Figure S2).

The Φ_f of the PbS Qdot is determined using the IR-26 dye dissolved in 1,2-dichloroethane (DCE) as reference standard via eq 2.

$$\Phi_s = \Phi_{ref} \times (I_s/I_{ref}) \times (A_{ref}/A_s) \times (n_s/n_{ref})^2 \quad (2)$$

Here the subscripts "s" and "ref" denote sample and reference, I is the integrated emission intensity, A is the absorbance at the excitation wavelength, and n is the refractive index of the solvent. Using a recently reported Φ_{ref} of 0.11% for the IR-26 dye,[17] the Φ_f of the RNase-A@PbS Qdot prepared at 80 °C is determined as 17.3%, placing it as one of the brightest water-soluble NIR-II emitting Qdots. It should be noted that there is a big discrepancy regarding the Φ_f of IR-26 dye reported in literature. For example, Murphy et al. claimed Φ_f = 0.5% for the dye (which was widely quoted),[19] while Semonin et al. determined the value as 0.048%,[18] and more recently, Hatami et al. reported a solvent absorption corrected value of 0.11%,[17] which we believe is the most accurate. Since significantly discrepant Φ_f values (>10-fold variation) of IR-26 are quoted in literature, it is difficult to compare the Φ_f of different NIR-II Qdots. Therefore, we have normalized the literature values using Φ_{ref} = 0.11% for the IR-26 reference, and the results are summarized in Table 1. It reveals that the as-prepared PbS Qdot has the highest normalized Φ_f among the currently available NIR-II Qdots in aqueous solution. It is ~2.7-fold as high as that of the C18−PMH-PEG@Ag_2Se Qdot that has already been regarded as one of brightest water-soluble NIR-II Qdots.[15] The high Φ_f of RNase-A@PbS Qdots together with λ_{em} of ~1300 nm (corresponding to tissue absorption minimum) should allow for deep optical tissue penetration and ultrahigh sensitivity pertaining to *in vivo* fluorescence imaging.[9]

DOI: 10.1021/acs.chemmater.6b00208
Chem. Mater. 2016, 28, 3041−3050

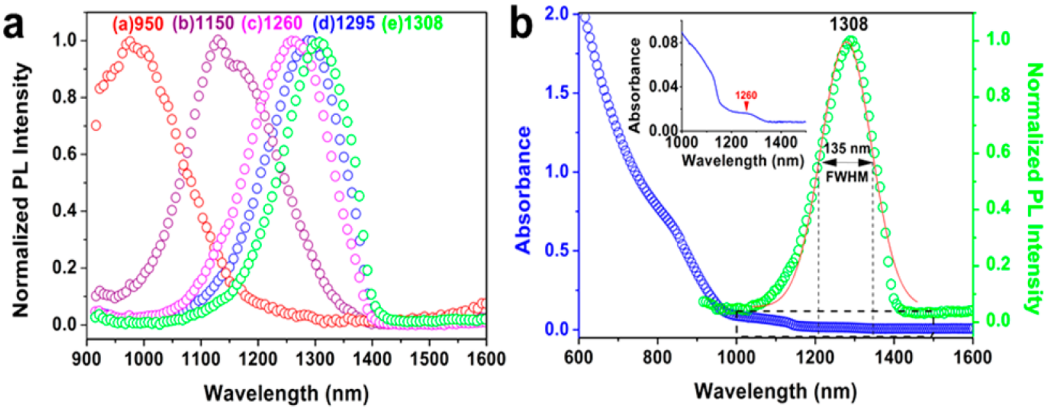

Figure 1. (a) Photoluminescence (PL) spectra of color-tunable RNase-A@PbS Qdots excited at a fixed wavelength λ_{ex} = 785 nm. (b) UV/vis/NIR absorption and PL spectra of the Qdot with an emission maximum peaking at 1308 nm. The PL spectrum is fitted to a Gaussian function (R^2 = 0.976), giving a fwhm of 135 nm. Inset shows a zoom-in graph of the NIR absorption ranging from 1000 to 1500 nm; the first excitonic absorption peak at 1260 nm is pointed with an arrowhead (red).

Table 1. Comparison of Typical Fluorescence Properties (Tunable Emission Peak λ_{em} Range, Emission FWHM, and Φ_f) of Typical Water-Soluble NIR-II Emitting Qdots

Qdot sample (coating@core)	reported Φ_f (%)	normalized Φ_f[a] (%)	λ_{em} range (nm)	fwhm (nm)	ref
DHLA@Ag_2S	6.9	1.3	1200	~170	14
PEG@Ag_2S	15.5	3.4	1200	~170	14
C18−PMH-PEG@Ag_2Se	29.4	6.5	1300	~170	15
GSH@PbS	6−16	?	~900−1230	210−260	16
GST-EGFP-GB1@PbS	10	?	1150	~250	26
RNase-A@PbS	17.3	17.3	1300	135	this work

[a]Normalized Φ_f is obtained using a Φ_f of 0.11% for the IR-26 reference standard.

A dense, robust surface coating on the PbS Qdot is essential for high colloidal stability and for providing effective protection for the core (retaining high fluorescence) to prevent possible leakage of toxic Pb^{2+} ions,[32] which is crucial for *in vivo* applications. Although galena has an extremely low solubility product constant (K_{sp} = 4 × 10^{-28} mol^2 dm^{-6}) that ensures minimal Pb^{2+} leakage due to natural solubility, the high level of intracellular thiol-containing small molecules (*e.g.*, cysteine ~1 mM)[22] can potentially etch the core if it is not well-protected, compromising its fluorescence,[33] and causing cytotoxicity (via released Pb^{2+} ions). Against all expectations, the RNase-A@PbS Qdot has robust resistance to cysteine etching: exposure to high concentrations of cysteine *in vitro* (up to 20 mM, ~20 times the level of intracellular cysteine content) does not weaken the fluorescence (Figure S3). Presumably the protein molecules may form a dense coating on the Qdot's surface that safeguards the core from cysteine etching. Besides, fluorescence stability of the Qdot in three commonly used biological media, *i.e.*, PBS, FBS, and DMEM is further investigated (see Figures S4 and S5 and the relevant discussion of the mechanism in SI).

Structure and Core-Size Characterization. Transmission electron microscopy (TEM) provides accurate measurement of size and morphology of nanomaterials, especially those containing heavy metals. Figure 2a shows that the as-prepared PbS Qdots are mostly spherical. Further examination on an individual particle based on high-resolution (HR) TEM imaging reveals a highly crystalline structure with an interplanar spacing of 0.295 nm (Figure 2a, inset), in agreement with the expected d_{200} distance of face centered cubic (fcc) PbS structure (JCPDS 5-592: unit cell length a_0 = 0.5934 nm, theoretical d_{200} = $1/2a_0$ = 0.297 nm). However, the edges of smaller Qdots are not easily distinguished from the background

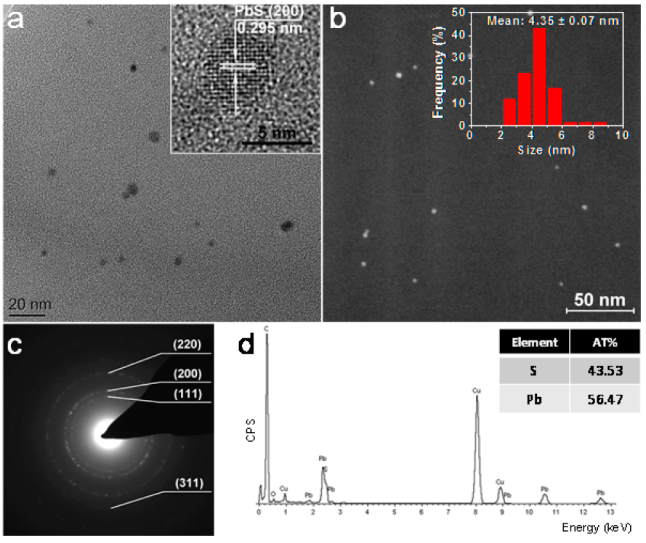

Figure 2. (a) TEM image of the as-synthesized PbS Qdots. Inset shows high-resolution TEM (HR-TEM) image of an individual Qdot. (b) High-angle annular dark-field scanning transmission electron microscopy (HAADF-STEM) image showing the Qdots as bright spots. Inset shows size histogram of a hundred particles, giving an average size of 4.35 ± 0.07 nm. (c) Selected area electron diffraction (SAED) pattern. The labeled rings are assigned to crystal lattice diffractions of a face centered cubic PbS structure. (d) Energy dispersive X-ray spectroscopy (EDX) spectrum showing elements presented in the sample (Pb:S atomic ratio = 56:44).

due to low bright-field (BF) contrast, impeding the accurate size determination. Thereupon, a coherent image is obtained

DOI: 10.1021/acs.chemmater.6b00208
Chem. Mater. 2016, 28, 3041−3050

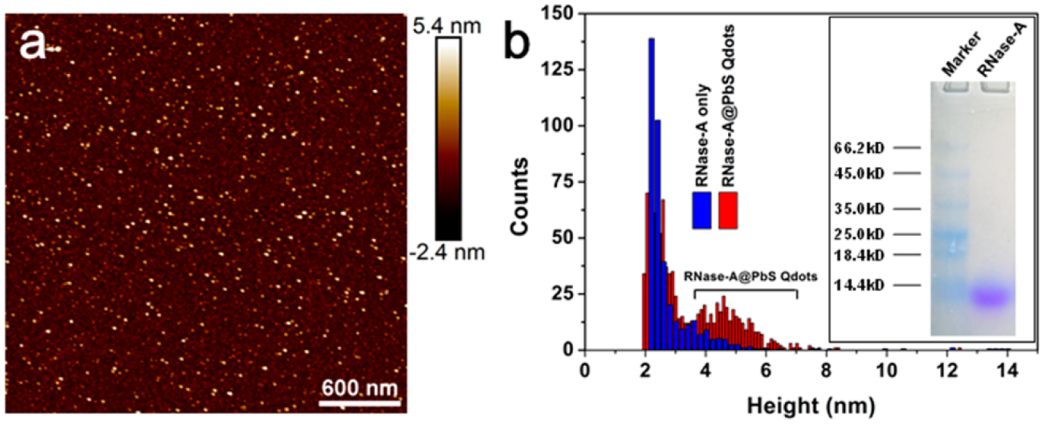

Figure 3. (a) Representative atomic force microscopy (AFM) topographic image of RNase-A@PbS Qdots deposited on a flat mica with a dilution of 1:1000. (b) Corresponding height distribution histogram of RNase-A@PbS Qdots (red bar) and RNase-A only (blue bar). Inset shows gel electrophoresis analysis of molecular weight marker (left lane) and pure RNase-A (right lane) which has undergone the identical process for the Qdot synthesis.

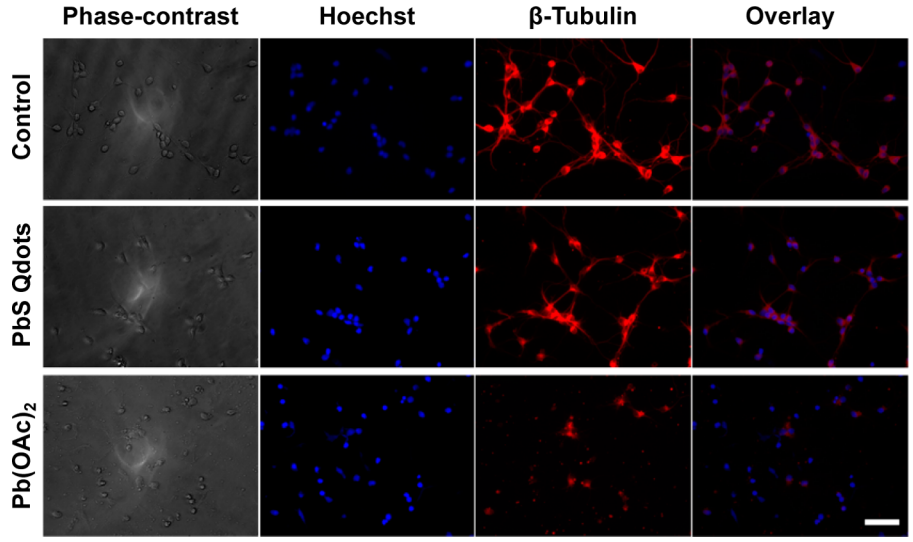

Figure 4. Phase-contrast, fluorescence, immune-fluorescence, and overlay micrographs (left to right columns) of fetal rat cortical neuronal cells incubated with PBS (healthy control, top row), RNase-A@PbS Qdots (middle row, 1 μM), and $Pb(OAc)_2$ (bottom row, 0.5 μM) for 24 h. Nuclei are stained with Hoechst 33342 (shown in blue); cell bodies, dendrites, and axons are tagged with monoclonal anti-β-tubulin antibody (shown in red). Scale bar represents 100 μm.

with a high-angle annular dark-field scanning TEM (HAADF-STEM) using Z-contrast imaging mode wherein the intensity is proportional to atomic number $Z^{1.7}$.[29] In the STEM image, the Qdots appear as "white" spots against "black" background after flattening, providing better contrast (Figure 2b). An analysis on 100 Qdots gives an average diameter of 4.35 ± 0.07 nm (polydispersity index σ = 25.1%, Figure 2b, inset) that matches perfectly to the calculated result via eq 1 (*ca.* 4.44 nm, see previous section). Therefore, each Qdot core is calculated to contain ~824 PbS formula units (for an fcc structure as confirmed by HR-TEM), yielding an equivalent PbS core weight of 1.97×10^5 Da (see SI for detailed calculation). Using the relationship between extinction coefficient (ε) of the first excitonic transition and PbS Qdot radius (r) reported by Cademartiri et al.,[31] ε here is determined to be 1.18×10^5 M^{-1} cm^{-1} at 1260 nm, giving a concentration of ~130 nM for the as-synthesized RNase-A@PbS Qdots. Figure 2c shows the corresponding selected area electron diffraction (SAED) pattern in which the diffraction rings are indicative of randomly orientated Qdots with an fcc PbS structure. Energy-dispersive X-ray spectroscopy (EDX) confirms the presence of Pb and S elements with an approximate atomic ratio of 1:1 (Figure 2d).

Since it is unavailable for the protein/organic shell detection by TEM, atomic-force microscopy (AFM) was utilized to monitor the overall dimension of RNase-A@PbS Qdots.[36] Figure 3a presents an AFM topographic image (tapping mode in water, after 1:1000 dilution of the freshly prepared stock solution) of well-dispersed spherical Qdots with height profiles ranging from *ca.* 2−8 nm (with height <2 nm removed to cut off background noise). The height histogram shows two distinct species: one appears at ~2.5 ± 0.4 nm (mean ±1/2FWHM) and the other at ~5.0 ± 0.6 nm (Figure 3b). Compared to the height distribution of RNase-A only, the former can be assigned to free RNase-A (expected molecular size $2.2 \times 2.8 \times 3.8$ nm^3),[35] the amount of which is in excess, while the latter is presumably due to the incorporation of PbS Qdot into the protein. To assess whether aggregates account for the larger species, a control sample of RNase-A only is

DOI: 10.1021/acs.chemmater.6b00208
Chem. Mater. 2016, 28, 3041−3050

treated under the identical Qdot synthesis condition. As shown in Figure 3b, inset, gel electrophoresis analysis disproves the coformation of dimeric and/or multimertic RNase-As as well as their possible contribution to the higher height profiles observed in the AFM image.[29]

Cytotoxicity Investigation. Lead exposure is the biggest safety concern for any lead-containing reagents with regard to *in vivo* applications. Bischoff et al. reported that the toxicity of lead given intravenously has a high correlation to its form, with the ionic lead being the most poisonous.[21,37] Indeed, lead can adversely affect every organ in the body, especially the central nerve system that is most sensitive to lead-induced toxicity.[21] Therefore, we compared the cytotoxicity of RNase-A@PbS Qdots with $Pb(OAc)_2$ toward fetal rat cortical neurons. Figure 4 shows the immunofluorescent analysis of neuronal cells treated with PBS, RNase-A@PbS Qdots, and $Pb(OAc)_2$ for 24 h. The nuclei stained with Hoechst 33342 appear in blue while the cell bodies, dendrites, and axons are stained with monoclonal anti-β-tubulin antibodies which emit red.[38] Similar to the healthy control, the neurons incubated with a high dose of the Qdots (~1 μM, equivalent to total Pb^{2+} concentration = 824 μM) are found to form a neurite network without any observable debris, suggesting minimal neurotoxicity. On the contrary, the neurite growth and network formation are downright inhibited by 0.5 μM $Pb(OAc)_2$, at a concentration that is >1600-fold lower than the total lead content contained in the Qdot sample. Conclusively, this result further confirms that the protein layer effectively prevents the release of lead content from the PbS Qdot.

The effects of the Qdots on cell apoptosis rate and cycle distribution are investigated using human gastric epithelial GES-1 (normal) and A375 human malignant melanoma (cancer) cells. An Annexin V/allophycocyanin (APC) and propidium iodide (PI) dual-color staining assay is utilized to examine apoptosis and necrosis rate of the cells.[39] Compared to the healthy control, the Qdot-treated cells do not show a significant increase of necrotic and apoptotic cell populations even at a high dose of 26 nM (equivalent Qdot weight dosage ~5.2 mg/L). The percentages of normal cells are determined to be 89.6%, 89.7%, 92.7%, 91.4%, and 94.5% after 24 h treatment with 0, 1.3, 2.6, 13, and 26 nM Qdots, respectively. None of these values differ significantly from the healthy control (89.6%, Figure 5a), indicating that the Qdot is nontoxic over the above dose range. Moreover, a further MTT-based cell proliferation analysis on three different cell lines including GES-1, human embryonic kidney (293T), and human malignant melanoma (A375) cells reveals no significant decrease in cell viability after 24 h Qdot incubation (see SI, Figure S9).[30,34] As shown in Figure 5b, the Qdot treatments cause a dose-dependent, small increase of cell population at the S-phase (increased from 12.6% to 15.8% at 26 nM) while there is a decrease at the G0/G1 phases (decreased from 87.1% to 82.8% at 26 nM). Such quantitative data indicate that treatment with a relatively high level of Qdot appears to promote DNA replication in GES-1 cells. Similar results are also found for the Qdot treated A375 cells (see Figure S8). Accordingly, all of these cellular evaluation results reveal a non-cytotoxicity/low cytotoxicity of the RNase-A@PbS Qdots under such *in vitro* conditions. We attribute the excellent biocompatibility to the effective protection of the Qdot by a dense protein coating which minimizes the release of biologically active Pb^{2+} ions.

Qdot for Tissue and *in Vivo* NIR-II Imaging. A simulated *ex vivo* experiment is performed to determine the maximal

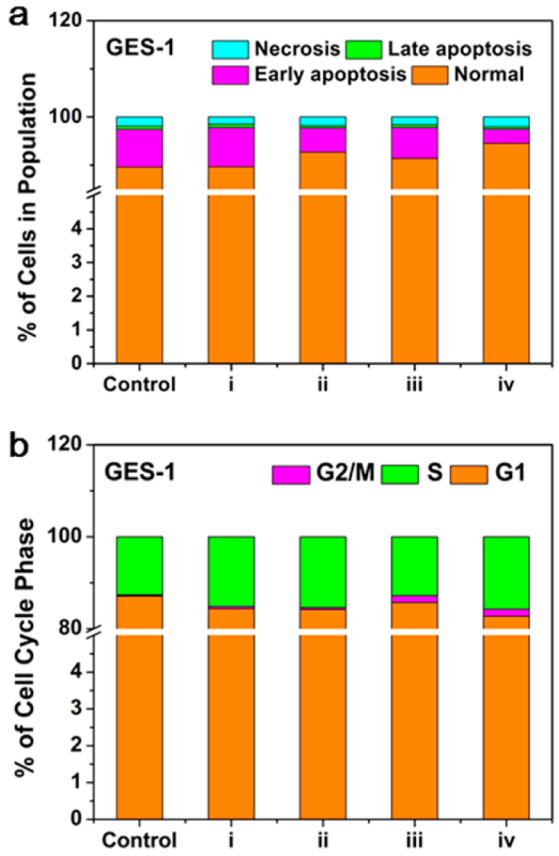

Figure 5. Apoptosis/necrosis and cell cycle distribution of GES-1 cells treated with varying concentrations of RNase-A@PbS Qdots (control to iv represent 0, 1.3, 2.6, 13, and 26 nM of Qdot, respectively) for 24 h. (a) Quantitative percentage representation of normal, early, and late apoptotic, and necrotic cells based on an Annexin V-APC/PI dual-staining assay. (b) Histogram showing the percentage of cells in each phase of the cell cycle.

tissue penetration using a pork muscle tissue as a phantom. First, various dosages of the Qdots (50 μL each) are injected into the tissue at an identical depth of 0.5 cm. The NIR-II image reveals a positive linear correlation between the ROI intensity and the Qdot concentration from 5 to 130 nM with a detection threshold concentration of ~5 nM (SI, Figure S10). We note, however, the muscularly deposited Qdots will diffuse along muscle fibers, and therefore, the actual threshold concentration should be less than 5 nM. Figure 6a,b shows an optical and NIR-II fluorescence image (false color) of the pork muscle injected with a fixed amount of Qdots (50 μL, 130 nM) at different depths (*ca.* 0.5, 1, 1.5, and 2 cm), respectively. The spot at 0.5 cm deep gives the strongest fluorescence whereas that at 2 cm is barely detectable. The ROI intensity as a function of injection depth demonstrates a perfect single exponential decay (R^2 = 0.999) with a δ value (tissue thickness for fluorescence decaying to 1/e) of 0.41 cm (Figure 6c). Such a relationship is exactly what is expected from the Beer–Lambert law of absorption. As shown in Figure 6b, such small quantities of the Qdots (~6.5 pmol, or ~1.3 μg core weight) can provide a detectable signal at an imaging depth of 1.5 cm in pork muscle. Such an impressive tissue imaging depth is benefitted from its high Φ_f peaking at ~1300 nm, a wavelength that provides the deepest tissue penetration.[9,11,15]

The *ex vivo* studies have proved the great potential of RNase-A@PbS Qdots for sensitive and low-dose *in vivo* imaging.

DOI: 10.1021/acs.chemmater.6b00208
Chem. Mater. 2016, 28, 3041−3050

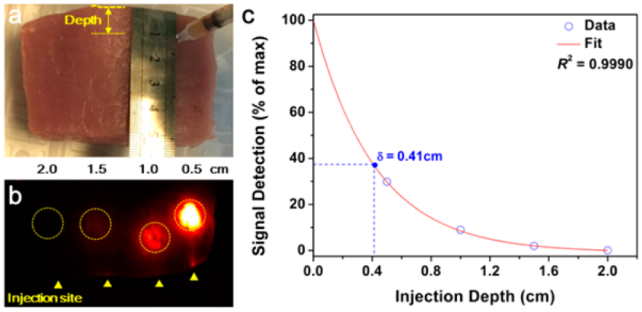

Figure 6. (a) Front-view optical image of a pork muscle tissue with 50 μL ~ 130 nM RNase-A@PbS Qdots being injected at different depths of 0.5, 1, 1.5, and 2 cm. (b) Top-view fluorescence image of the tissue. (c) NIR-II fluorescence as a function of injection depth. The data (blue dots) are fitted to a first-order exponential decay (red line) via the equation: $I/I_0 = -0.00819 + 1.00819e^{-2.3804d}$, where I/I_0: ROI intensity ratio, and d is injection depth, giving δ = 0.41 cm.

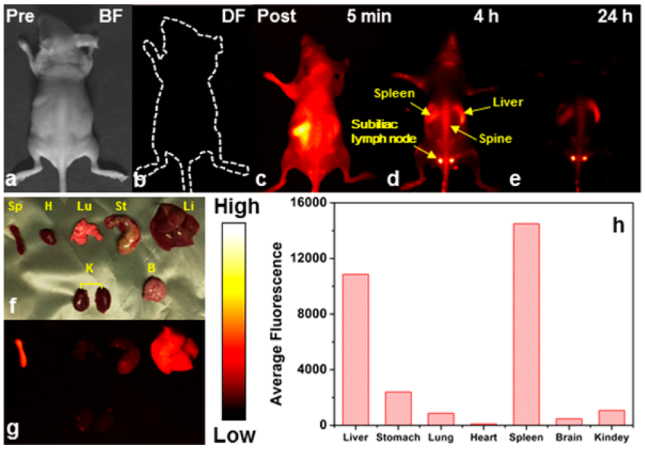

Figure 7. RNase-A@PbS Qdots for *in vivo* NIR-II fluorescence imaging. (a) Dorsal bright-field and (b) fluorescence images of a living nude mouse at preinjection. (c–e) Time-course fluorescence images after intravenous injection of the Qdots (200 μL, 26 nM) into the mouse illuminated under an 808 nm diode laser (power density, 15 mW/cm^2; exposure time, 100 ms). Spine, subiliac lymph node, spleen, and liver (yellow arrowheads) give the strongest signals. *Ex vivo* (f) white-light and (g) fluorescence images of major organs harvested at 24 h postinjection. Abbreviations are Sp, spleen; H, heart; Lu, lung; St, stomach; Li, liver; K, kidney; B, brain. (h) Average fluorescence intensity of organs.

Thereupon, we pretest the *in vivo* imaging by intramuscularly injecting 20 μL of the Qdots (26 nM) into a mouse's leg muscle at a depth of ~0.5 cm. The corresponding NIR-II fluorescence image is captured with an InGaAs CCD camera under the radiation of an 808 nm diode laser (15 mW/cm^2). This laser power density is well below the exposure limit (329 mW/cm^2) for skin defined by the International Commission on Nonionizing Radiation Protection (ICNIRP). The overlaid optical and fluorescence images (Figure S11) show a bright spot around the injection site with nearly zero autofluorescence background apart from the rest of the body, suggesting the Qdot is well-suited for sensitive *in vivo* imaging. The biodistribution and imaging studies of the RNase-A@PbS Qdots are performed on nude mice (n = 3) by intravenous administration.[38] Prior to injection, the mouse displays negligible fluorescence background under 808 nm laser excitation (Figure 7b), whereas an intense fluorescence signal is detected in the superficial vasculature throughout the mouse's body at 5 min postinjection of the Qdots (200 μL at 26 nM, total Qdot dose = 5.2 pmol or ~1.0 μg core weight), with the strongest signal appearing in the spleen (Figure 7c). Over time though, the signals entirely fade except for the spleen, liver, spine, and subiliac lymph nodes (Figure 7d,e). The lymph nodes remain very bright at 24 h postinjection, indicating strong preferential accumulation of the Qdots in such organs. An *ex vivo* study of major organs harvested at 24 h postinjection also confirms the Qdots' preferential accumulation in the mouse's spleen and liver (Figure 7f,g), which display much higher average ROI intensities than other organs (*e.g.*, heart, brain, kidney, lung *etc.*, Figure 7h). It is well-known that nanometer sized objects are preferentially excreted via the reticuloendothelial system (RES, *e.g.*, spleen, liver, and lymph nodes) *in vivo*.[40,41] Besides the RES organs, the Qdots are found to accumulate considerably in the skeleton, especially the spinal column. As shown in Figure 8a, the mouse's bone structures (*e.g.*, lumbar vertebrae, sacral vertebrae, caudal vertebrae, humerus, phalanges, *etc.*) are clearly identified with the excellent contrast appearing at 1 h postinjection. Moreover, an X-ray image of the mouse's skeleton is presented for comparison (see Figure 8b). A cross-sectional analysis upon ROI intensity gives a diameter of 0.289 cm for the C5 vertebra, matching well to the corresponding X-ray measurement (Figure 8c,d). This result represents a remarkable example of a fluorescence imaging probe that can clearly map an animal's bone structures without the need of a bone-targeting agent and/or necropsy. Regarding the mechanism behind this phenomenon, we speculate that the specific accumulation of Qdots in bones is presumably due to high uptake by bone marrow macrophages.[42] This result thus reveals a potential application of the RNase@Qdot for bone fracture and dislocation diagnosis. More importantly, the Qdot dose per mouse used is about 5.2 pmol (or ~1 μg core weight), which is substantially lower (by ~40–600 fold) than other NIR-II emitting Qdots used for *in vivo* imaging (see Table 2). This ultralow dosage is a clear reflection of superior brightness of our RNase-A@PbS Qdot, which is important to reduce the risk of potential lead exposure.

The biokinetics of intravenously injected Qdots (freshly prepared) is determined by inductively coupled plasma-mass spectrometry (ICP-MS) from collected blood samples at various postinjection time points (n = 2 mice). For effective *in vivo* targeting applications, the injected Qdots should avoid rapid clearance from the body to keep the concentration high enough in the bloodstream for tissue perfusion. On the other hand, however, a long Qdot plasma half-life can lead to a persistent exposure to the potentially harmful content (Pb in this study) to pose a health risk. As shown in the blood circulation curve (Figure 9), the half-life ($t_{1/2}$) of the RNase-A@PbS Qdot is determined to be 4.17 h, a reasonable value. Theoretically, four cycles (or 4 × $t_{1/2}$ periods) permit the elimination of the injected dose by ~94%.[43] Therefore, we anticipate that almost all of the injected Qdots are cleared from the bloodstream within ~17 h, in good agreement with the observation that almost no blood retention of the Qdot as indicated in Figure 9. Although the size of the as prepared Qdot (Figure 3b) matches closely to the size threshold (*ca.* 5.5 nm) for renal filtration, the adsorption of serum proteins on such negatively charged Qdots during blood circulation may increase its D_h to above the renal clearance threshold as revealed from the increased major component size of ~90 nm in serum media

DOI: 10.1021/acs.chemmater.6b00208
Chem. Mater. 2016, 28, 3041–3050

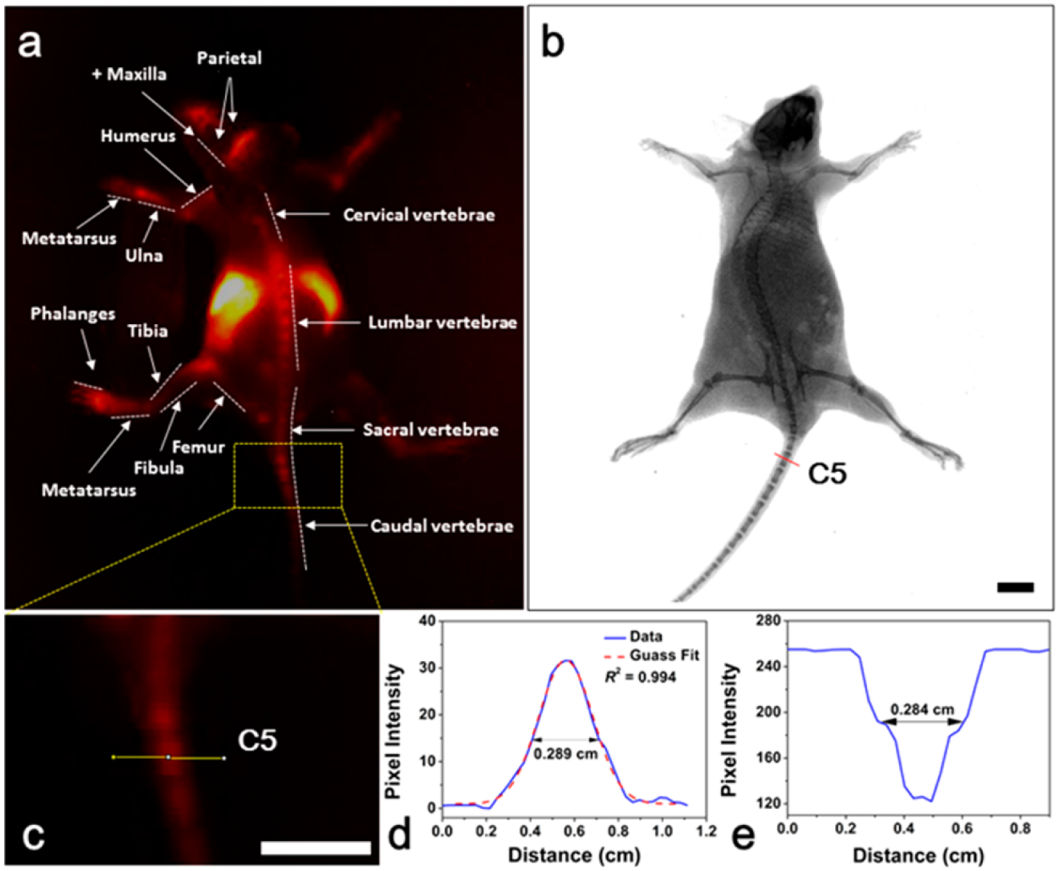

Figure 8. (a) NIR-II fluorescence image of a living nude mouse at 1 h postinjection for mapping major bone structures (identified with arrows). (b) X-ray image. (c) A zoom-in image of the selected area in part a. (d) A cross-sectional intensity profile measured along the yellow line in part c is fitted to a Gaussian function. (e) A cross-sectional intensity profile measured along the red line in part b. Scale bars represent 1 cm.

Table 2. Comparison of Typical Dosages per Mouse Used for NIR-II Emitting Qdots for *in Vivo* Fluorescence Imaging

Qdot (coating@core)	dose (pmol)	dose (μg)	ref
6PEG@Ag_2S	750	268	12
C18−PMH-PEG@Ag_2Se	?	120	15
GSH-anti-HER2@PbS	?	600	16
PEG@Ag_2S	?	300	23
GST-EGFP-GB1@PbS	200	?	26
RNase-A@PbS	5.2	~1.0	this work

(FBS, see Figures S6 and S7).[44] Such enlarged protein-Qdots should normally end up in RES including liver and spleen (in good accordance with the fluorescence image observed in Figure 7g), and would be mainly excreted through the biliary pathway into feces.[45] Therefore, the Qdot contents from both the urine and feces excretes are collected with metabolism cages over an 18-day period. The ICP-MS-based quantitative analysis confirms that time-dependent fecal excretion is the predominant pathway for the clearance of the injected Qdots from the body with negligible excretion from urine (Figure S12). Furthermore, little retention of the Qdots in other major organs is observed (see Figure 7), which is important for minimizing the long-term toxicity. Indeed, as shown in Figure 10, neither injury nor inflammation that reflects acute toxicity is noted for the hematoxylin and eosin (H&E) stained organ tissues at day-18 postinjection as compared to the control (injected with sterile saline), confirming that the Qdot at such a dosage does not induce any significant toxicity.

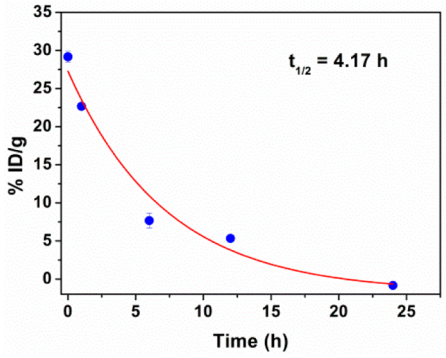

Figure 9. Blood concentration (percentage of injected dose per gram of tissue, %ID/g) of RNase-A@PbS Qdots after intravenous injection (200 μL, ~ 26 nM) into mice, as measured by ICP-MS at various time points. The data are fitted to a first-order exponential decay (R^2 = 0.9788) with a blood half-life of 4.2 h (n = 2). Note that an orbital bleeding method is used for blood collection with capillary tubes.

CONCLUSIONS

In summary, a microwave assisted approach has been developed for rapid synthesis of well-dispersed, highly fluorescent, and biocompatible RNase-A capped PbS Qdots in aqueous phase. Owing to its far superior brightness in the NIR-II region, the Qdot provides deep tissue penetration with excellent contrast at an ultralow dosage of 5.2 pmol (~1 μg) per mouse, which is a substantial 40−600-fold lower than

DOI: 10.1021/acs.chemmater.6b00208
Chem. Mater. 2016, 28, 3041−3050

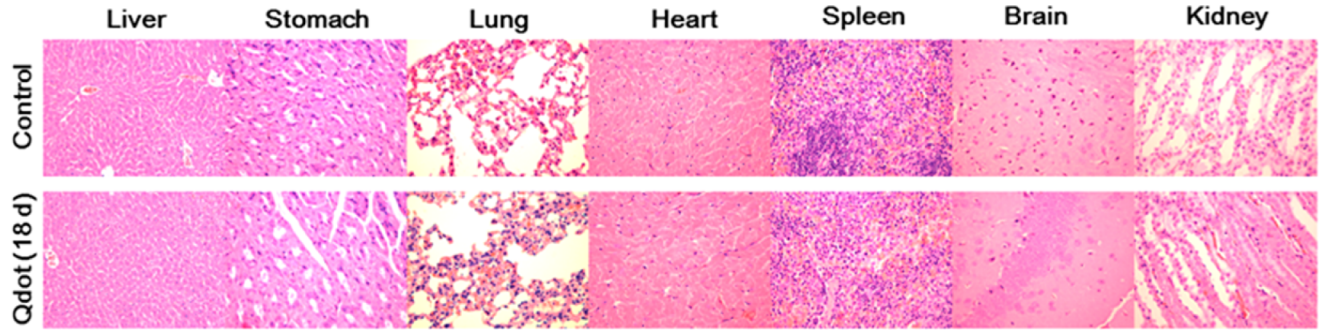

Figure 10. Representative histological H&E staining of major organ tissues harvested from the mice treated with sterile saline (control) and RNase-A@PbS Qdot for 18 days (magnification: ×400).

typical dosages used by other literature NIR-II Qdots. Moreover, the Qdots not only display negligible cytotoxicity but also ready RES excretion from the body, suggesting minimal long-term toxicity *in vivo*. Further coupling of specific targeting and/or therapeutic agents to the NIR-II Qdot will allow the construction of a multifunctional theranostic nanoplatform for simultaneous tumor diagnosis and therapeutic applications.

■ ASSOCIATED CONTENT

Supporting Information

The Supporting Information is available free of charge on the ACS Publications website at DOI: 10.1021/acs.chemmater.6b00208.

Cell culture experimental details, results of assays, and additional results presented with figures (PDF)

■ AUTHOR INFORMATION

Corresponding Authors

*E-mail: cshiyi@163.com.
*E-mail: d.zhou@leeds.ac.uk.

Author Contributions

Y.K., J.C., and D.Z. conceived the idea and designed the experiments. Y.K., J.C., H.F., G.H. and W.W. performed the research. Y.K. and D.Z. analyzed data. Y.K. and D.Z. wrote the paper. All authors have read, commented, and approved the final version of the paper. Y.K. and J.C. contributed equally.

Notes

The authors declare no competing financial interest.

■ ACKNOWLEDGMENTS

We thank Dr. Michael Ward (University of Leeds) for help in TEM imaging and Dr. Yueming Wang (School of Medicine, Shanghai Jiao Tong University) for suggestions and help in rat cortical neuron culture. Y.K. thanks University of Leeds for providing a Fully-Funded International Research Scholarship (FFIRS). Y.G. thanks the Wellcome Trust (UK) for providing a career re-entry fellowship (Grant No: 097354/Z/11/Z). This work was supported by the University of Leeds (UK), Huashan Hospital (China), and the Royal Society-International Exchange Scheme (2014 China NSFC cost-share), and also in part by the National 863 Hi-Tech Project (2015AA033703), National Natural Science Foundation of China (Nos. 81271958, 81301672, 81401771, 81201773, and No. 21171117 to Dr Feng Gao from SJTU), Natural Science Foundation of Shanghai Project (No. 12ZR1415800 and No. 15ZR1405000), the Specialized Research Fund for the Doctoral Program of Higher Education (No. 20120071110067), China Postdoctoral Science Foundation (No. 2014M560296), and Innovation Program of Shanghai Municipal Education Commission (No. 15ZZ006).

■ REFERENCES

(1) Bruchez, M.; Moronne, M.; Gin, P.; Weiss, S.; Alivisatos, A. P. Semiconductor Nanocrystals as Fluorescent Biological Labels. *Science* **1998**, *281*, 2013−2016.

(2) Chan, W. C. W.; Nie, S. M. Quantum Dot Bioconjugates for Ultrasensitive Nonisotopic Detection. *Science* **1998**, *281*, 2016−2018.

(3) Medintz, I. L.; Clapp, A. R.; Mattoussi, H.; Goldman, E. R.; Fisher, B.; Mauro, J. M. Self-Assembled Nanoscale Biosensors Based on Quantum Dot FRET Donors. *Nat. Mater.* **2003**, *2*, 630−638.

(4) Wu, X. Y.; Liu, H. J.; Liu, J. Q.; Haley, K. N.; Treadway, J. A.; Larson, J. P.; Ge, N. F.; Peale, F.; Bruchez, M. P. Immunofluorescent Labeling of Cancer Marker Her2 and Other Cellular Targets with Semiconductor Quantum Dots. *Nat. Biotechnol.* **2003**, *21*, 41−46.

(5) Michalet, X.; Pinaud, F. F.; Bentolila, L. A.; Tsay, J. M.; Doose, S.; Li, J. J.; Sundaresan, G.; Wu, A. M.; Gambhir, S. S.; Weiss, S. Quantum Dots for Live Cells, In Vivo Imaging, and Diagnostics. *Science* **2005**, *307*, 538−544.

(6) Smith, A. M.; Mancini, M. C.; Nie, S. Bioimaging: Second Window for In Vivo Imaging. *Nat. Nanotechnol.* **2009**, *4*, 710−711.

(7) Welsher, K.; Liu, Z.; Sherlock, S. P.; Robinson, J. T.; Chen, Z.; Daranciang, D.; Dai, H. A Route to Brightly Fluorescent Carbon Nanotubes for Near-Infrared Imaging in Mice. *Nat. Nanotechnol.* **2009**, *4*, 773−780.

(8) Du, Y.; Xu, B.; Fu, T.; Cai, M.; Li, F.; Zhang, Y.; Wang, Q. Near-Infrared Photoluminescent Ag_2S Quantum Dots from a Single Source Precursor. *J. Am. Chem. Soc.* **2010**, *132*, 1470−1471.

(9) Lim, Y. T.; Kim, S.; Nakayama, A.; Stott, N. E.; Bawendi, M. G.; Frangioni, J. V. Selection of Quantum Dot Wavelengths for Biomedical Assays and Imaging. *Mol. Imaging* **2003**, *2*, 50−64.

(10) Welsher, K.; Sherlock, S. P.; Dai, H. J. Deep-Tissue Anatomical Imaging of Mice using Carbon Nanotube Fluorophores in the Second Near-Infrared Window. *Proc. Natl. Acad. Sci. U. S. A.* **2011**, *108*, 8943−8948.

(11) Hong, G.; Lee, J. C.; Robinson, J. T.; Raaz, U.; Xie, L.; Huang, N. F.; Cooke, J. P.; Dai, H. Multifunctional In Vivo Vascular Imaging using Near-Infrared II Fluorescence. *Nat. Med.* **2012**, *18*, 1841−1846.

(12) Hong, G.; Robinson, J. T.; Zhang, Y.; Diao, S.; Antaris, A. L.; Wang, Q.; Dai, H. In Vivo Fluorescence Imaging with Ag_2S Quantum Dots in the Second Near-Infrared Region. *Angew. Chem., Int. Ed.* **2012**, *51*, 9818−9821.

(13) Robinson, J. T.; Hong, G.; Liang, Y.; Zhang, B.; Yaghi, O. K.; Dai, H. In Vivo Fluorescence Imaging in the Second Near-Infrared Window with Long Circulating Carbon Nanotubes Capable of Ultrahigh Tumor Uptake. *J. Am. Chem. Soc.* **2012**, *134*, 10664−10669.

(14) Zhang, Y.; Hong, G.; Zhang, Y.; Chen, G.; Li, F.; Dai, H.; Wang, Q. Ag_2S Quantum Dot: A Bright and Biocompatible Fluorescent

DOI: 10.1021/acs.chemmater.6b00208
Chem. Mater. 2016, 28, 3041−3050

Nanoprobe in the Second Near-Infrared Window. *ACS Nano* **2012**, *6*, 3695−3702.
(15) Dong, B.; Li, C.; Chen, G.; Zhang, Y.; Zhang, Y.; Deng, M.; Wang, Q. Facile Synthesis of Highly Photoluminescent Ag_2Se Quantum Dots as a New Fluorescent Probe in the Second Near-Infrared Window for In Vivo Imaging. *Chem. Mater.* **2013**, *25*, 2503−2509.
(16) Nakane, Y.; Tsukasaki, Y.; Sakata, T.; Yasuda, H.; Jin, T. Aqueous Synthesis of Glutathione-Coated PbS Quantum Dots with Tunable Emission for Non-Invasive Fluorescence Imaging in the Second Near-Infrared Biological Window (1000−1400 nm). *Chem. Commun.* **2013**, *49*, 7584−7586.
(17) Hatami, S.; Wuerth, C.; Kaiser, M.; Leubner, S.; Gabriel, S.; Bahrig, L.; Lesnyak, V.; Pauli, J.; Gaponik, N.; Eychmueller, A.; Resch-Genger, U. Absolute Photoluminescence Quantum Yields of IR26 and IR-Emissive Cd1-xHgxTe and PbS Quantum Dots - method- and Material-Inherent Challenges. *Nanoscale* **2015**, *7*, 133−143.
(18) Semonin, O. E.; Johnson, J. C.; Luther, J. M.; Midgett, A. G.; Nozik, A. J.; Beard, M. C. Absolute Photoluminescence Quantum Yields of IR-26 Dye, PbS, and PbSe Quantum Dots. *J. Phys. Chem. Lett.* **2010**, *1*, 2445−2450.
(19) Murphy, J. E.; Beard, M. C.; Norman, A. G.; Ahrenkiel, S. P.; Johnson, J. C.; Yu, P. R.; Micic, O. I.; Ellingson, R. J.; Nozik, A. J. PbTe Colloidal Nanocrystals: Synthesis, Characterization, and Multiple Exciton Generation. *J. Am. Chem. Soc.* **2006**, *128*, 3241−3247.
(20) Hennequin, B.; Turyanska, L.; Ben, T.; Beltran, A. M.; Molina, S. I.; Li, M.; Mann, S.; Patane, A.; Thomas, N. R. Aqueous Near Infrared Fluorescent Composites Based on Apoferritin-Encapsulated PbS Quantum Dots. *Adv. Mater.* **2008**, *20*, 3592−3596.
(21) Truong, L.; Moody, I. S.; Stankus, D. P.; Nason, J. A.; Lonergan, M. C.; Tanguay, R. L. Differential Stability of Lead Sulfide Nanoparticles Influences Biological Responses in Embryonic Zebrafish. *Arch. Toxicol.* **2011**, *85*, 787−798.
(22) Yuan, X.; Tay, Y.; Dou, X.; Luo, Z.; Leong, D. T.; Xie, J. Glutathione-Protected Silver Nanoclusters as Cysteine-Selective Fluorometric and Colorimetric Probe. *Anal. Chem.* **2013**, *85*, 1913−1919.
(23) Zhang, Y.; Zhang, Y.; Hong, G.; He, W.; Zhou, K.; Yang, K.; Li, F.; Chen, G.; Liu, Z.; Dai, H.; Wang, Q. Biodistribution, Pharmacokinetics and Toxicology of Ag_2S Near-Infrared Quantum Dots in Mice. *Biomaterials* **2013**, *34*, 3639−3646.
(24) Li, C.; Zhang, Y.; Wang, M.; Zhang, Y.; Chen, G.; Li, L.; Wu, D.; Wang, Q. In Vivo Real-Time Visualization of Tissue Blood Flow and Angiogenesis using Ag_2S Quantum Dots in the NIR-II Window. *Biomaterials* **2014**, *35*, 393−400.
(25) Zhang, Y.; Liu, Y.; Li, C.; Chen, X.; Wang, Q. Controlled Synthesis of Ag_2S Quantum Dots and Experimental Determination of the Exciton Bohr Radius. *J. Phys. Chem. C* **2014**, *118*, 4918−4923.
(26) Sasaki, A.; Tsukasaki, Y.; Komatsuzaki, A.; Sakata, T.; Yasuda, H.; Jin, T. Recombinant Protein (EGFP-Protein G)-Coated PbS Quantum Dots for In Vitro and In Vivo Dual Fluorescence (Visible and Second-NIR) Imaging of Breast Tumor. *Nanoscale* **2015**, *7*, 5115−5119.
(27) Pichaandi, J.; van Veggel, F. C. J. M. Near-Infrared Emitting Quantum Dots: Recent Progress on Their Synthesis and Characterization. *Coord. Chem. Rev.* **2014**, *263*, 138−150.
(28) Ma, N.; Marshall, A. F.; Rao, J. Near-Infrared Light Emitting Luciferase via Biomineralization. *J. Am. Chem. Soc.* **2010**, *132*, 6884−6885.
(29) Kong, Y.; Chen, J.; Gao, F.; Brydson, R.; Johnson, B.; Heath, G.; Zhang, Y.; Wu, L.; Zhou, D. Near-Infrared Fluorescent Ribonuclease-A-Encapsulated Gold Nanoclusters: Preparation, Characterization, Cancer Targeting and Imaging. *Nanoscale* **2013**, *5*, 1009−1017.
(30) Kong, Y.; Chen, J.; Gao, F.; Li, W.; Xu, X.; Pandoli, O.; Yang, H.; Ji, J.; Cui, D. A Multifunctional Ribonuclease-A-Conjugated CdTe Quantum Dot Cluster Nanosystem for Synchronous Cancer Imaging and Therapy. *Small* **2010**, *6*, 2367−2373.
(31) Moreels, I.; Lambert, K.; Smeets, D.; De Muynck, D.; Nollet, T.; Martins, J. C.; Vanhaecke, F.; Vantomme, A.; Delerue, C.; Allan, G.; Hens, Z. Size-Dependent Optical Properties of Colloidal PbS Quantum Dots. *ACS Nano* **2009**, *3*, 3023−3030.
(32) Cedervall, T.; Lynch, I.; Lindman, S.; Berggard, T.; Thulin, E.; Nilsson, H.; Dawson, K. A.; Linse, S. Understanding the Nanoparticle-Protein Corona using Methods to Quantify Exchange Rates and Affinities of Proteins for Nanoparticles. *Proc. Natl. Acad. Sci. U. S. A.* **2007**, *104*, 2050−2055.
(33) Zhou, D. J.; Li, Y.; Hall, E. A. H.; Abell, C.; Klenerman, D. A Chelating Dendritic Ligand Capped Quantum Dot: Preparation, Surface Passivation, Bioconjugation and Specific DNA Detection. *Nanoscale* **2011**, *3*, 201−211.
(34) Muthuswamy, E.; Iskandar, A. S.; Amador, M. M.; Kauzlarich, S. M. Facile Synthesis of Germanium Nanoparticles with Size Control: Microwave *versus* Conventional Heating. *Chem. Mater.* **2013**, *25*, 1416−1422.
(35) Shang, W.; Nuffer, J. H.; Dordick, J. S.; Siegel, R. W. Unfolding of Ribonuclease A on Silica Nanoparticle Surfaces. *Nano Lett.* **2007**, *7*, 1991−1995.
(36) Zhou, D. J.; Bruckbauer, A.; Abell, C.; Klenerman, D.; Kang, D. J. Fabrication of Three-Dimensional Surface Structures with Highly Fluorescent Quantum Dots by Surface-Templated Layer-by-Layer Assembly. *Adv. Mater.* **2005**, *17*, 1243−1248.
(37) Bischoff, F.; Maxwell, L. C.; Evans, R. D.; Nuzum, R. F. Studies on the Toxicity of Various Lead Compounds Given Intravenously. *J. Pharmacol. Exptl. Therap.* **1928**, *34*, 85−109.
(38) Lv, L.; Guo, Y.; Shen, Y.; Liu, J.; Zhang, W.; Zhou, D.; Guo, S. Intracellularly Degradable, Self-Assembled Amphiphilic Block Copolycurcumin Nanoparticles for Efficient In Vivo Cancer Chemotherapy. *Adv. Healthcare Mater.* **2015**, *4*, 1496−1501.
(39) Tian, W.; Liu, J.; Guo, Y.; Shen, Y.; Zhou, D.; Guo, S. Self-Assembled Micelles of Amphiphilic PEGylated Rapamycin for Loading Paclitaxel and Resisting Multidrug Resistant Cancer Cells. *J. Mater. Chem. B* **2015**, *3*, 1204−1207.
(40) Owens, D. E.; Peppas, N. A. Opsonization, Biodistribution, and Pharmacokinetics of Polymeric Nanoparticles. *Int. J. Pharm.* **2006**, *307*, 93−102.
(41) Schipper, M. L.; Iyer, G.; Koh, A. L.; Cheng, Z.; Ebenstein, Y.; Aharoni, A.; Keren, S.; Bentolila, L. A.; Li, J.; Rao, J.; Chen, X.; Banin, U.; Wu, A. M.; Sinclair, R.; Weiss, S.; Gambhir, S. S. Particle Size, Surface Coating, and PEGylation Influence the Biodistribution of Quantum Dots in Living Mice. *Small* **2009**, *5*, 126−134.
(42) Ballou, B.; Lagerholm, B. C.; Ernst, L. A.; Bruchez, M. P.; Waggoner, A. S. Noninvasive Imaging of Quantum Dots in Mice. *Bioconjugate Chem.* **2004**, *15*, 79−86.
(43) Levison, M.; Levison, J. Pharmacokinetics and Pharmacodynamics of Antibacterial Agents. *Infect. Dis. Clin. North. Am.* **2009**, *23*, 791−vii.
(44) Choi, H.; Liu, W.; Misra, P.; Tanaka, E.; Zimmer, J.; Ipe, B.; Bawendi, M.; Frangioni, J. Renal Clearance of Quantum Dots. *Nat. Biotechnol.* **2007**, *25*, 1165−1170.
(45) Kreyling, W.; Abdelmonem, A.; Ali, Z.; Alves, F.; Geiser, M.; Haberl, N.; Hartmann, R.; Hirn, S.; Jimenez de Aberasturi, D.; Kantner, K.; Khadem-Saba, G.; Montenegro, J.-M.; Rejman, J.; Rojo, T.; Ruiz de Larramendi, I.; Ufartes, R.; Wenk, A.; Parak, W. J. In Vivo Integrity of Polymer-Coated Gold Nanoparticles. *Nat. Nanotechnol.* **2015**, *10*, 619−623.

DOI: 10.1021/acs.chemmater.6b00208
Chem. Mater. 2016, 28, 3041−3050